INSTITUTE OF PHYSICS PUBLISHING PLASMA PHYSICS AND CONTROLLED FUSION

Plasma Phys. Control. Fusion **44** (2002) 2339–2355 PII: S0741-3335(02)38339-8

Observation of neoclassical impurity transport in Ohmically heated plasmas of CDX-U low aspect ratio tokamak

V A Soukhanovskii[1,3], M Finkenthal[1,4], H W Moos[1], D Stutman[1], T Munsat[2], B Jones[2], D Hoffman[2], R Kaita[2] and R Majeski[2]

[1] Plasma Spectroscopy Group, Department of Physics and Astronomy, The Johns Hopkins University, Baltimore, Md 21218, USA
[2] Princeton Plasma Physics Laboratory, Princeton, NJ 08543, USA

E-mail: vlad@pppl.gov

Received 19 June 2002
Published 23 October 2002
Online at stacks.iop.org/PPCF/44/2339

Abstract

High β, good confinement and stability properties of the low aspect ratio tokamaks, or spherical tori (ST), have been predicted theoretically and preliminarily confirmed in several large experiments recently. This paper reports on impurity transport experiments carried out in ohmically heated plasmas of the small spherical torus CDX-U with the aspect ratio of $A \simeq 1.5$. Vacuum ultraviolet and soft x-ray multichannel spectroscopic diagnostics are used to measure intrinsic carbon, oxygen and radiated power radial brightness profiles in plasmas with $T_e(0) \simeq 60$–$80\,\mathrm{eV}$ and $n_e(0) \simeq 2 \times 10^{13}\,\mathrm{cm}^{-3}$. The measurements are performed in both magnetohydrodynamically dominated and quiescent phase of the plasmas. The properties of the observed low m/n modes, sawtooth oscillations, and ST-specific reconnection events are discussed in the context of particle transport. The measured impurity profiles are modelled using one-dimensional impurity transport code MIST and a collisional-radiative package CRMLIN. Impurity diffusion of $0.2\,\mathrm{m}^2\,\mathrm{s}^{-1} \leqslant D \leqslant 0.6\,\mathrm{m}^2\,\mathrm{s}^{-1}$ and convection velocity of $v \simeq 4$–$16\,\mathrm{m\,s}^{-1}$ are inferred from the modelling. These transport coefficients are very close to the neoclassical theory predictions obtained with the FORCEBAL code, which uses analytical plasma viscosity expressions valid for an arbitrary aspect ratio geometry. Neoclassical analysis indicates that both carbon and oxygen are in the collisional regime, and the Pfirsch–Schluter flux is the major fraction of the impurity flux. The causes of the observed strong non-diffusive transport are discussed, and it is concluded that the $\nabla n_i/n_i$ term, resulting from highly peaked ion density profile, makes the largest contribution to the inward pinch. Present analysis suggests that drift wave turbulence is reduced in CDX-U ohmically heated discharges within

[3] Present address: Princeton Plasma Physics Laboratory, Princeton, NJ, USA.
[4] Permanent address: Racah Institute of Physics, Hebrew University of Jerusalem, Jerusalem, Israel.

at least $r/a \leqslant 0.4$, however more refined measurements are needed to interpret the results in the framework of ST ion transport.

1. Introduction

The low aspect ratio tokamak, or spherical torus (ST), is a promising innovative concept in magnetically confined fusion [1]. The predicted high β and good confinement and stability properties [2] have been recently verified in several ST experiments [3, 4]. The ST specific physics subjects [5] have also stimulated the advances in current drive and plasma heating concepts [6, 7], non-inductive start-up scenarios [8, 9], and magnetohydrodynamic (MHD) instability research [10–12], Several ST features, namely the low toroidal field, hence large particle gyro-radii, and a large radial magnetic field gradient, may have a direct impact on the collisional and microstability properties of ST plasmas and lead to the particle and energy transport mechanisms different than those in conventional large aspect ratio tokamaks. Thus, transport properties of low aspect ratio plasmas of various sizes and confinement modes must be studied to enable the generalization and scalings of ST transport.

Significant progress has been made in fusion plasma research towards the understanding of both the neoclassical (collisional) [13–15] and the anomalous heat and particle transport mechanisms. The latter is attributed to drift-wave electromagnetic microinstabilities [16–18], and a large effort is being undertaken to develop plasma turbulence and fluctuation diagnostics (e.g. [19]). However, many transport regimes in tokamaks are still understood at the phenomenological level.

A study of impurity transport in the low aspect ratio tokamak CDX-U is presented. The CDX-U device is a small ST in Princeton Plasma Physics Laboratory. It has been dedicated to novel research subjects in plasma physics and plasma diagnostics [20–24]. Presently CDX-U is a leading toroidal plasma experiment for liquid wall–plasma interaction studies. Liquid lithium rail limiter and toroidal tray limiter experiments are underway. These experiments provide a compelling motivation to understand and document the MHD activity, transport and confinement properties of a standard ohmic CDX-U discharge, so that further comparisons can be made to the plasmas in the presence of the liquid lithium boundary interface.

Several multichannel vacuum ultraviolet (VUV) spectroscopic diagnostics are used in this work to measure intrinsic carbon and oxygen brightness profiles. Impurity density profiles n_{I} are derived and modelled self-consistently to obtain a range of valid transport coefficients as follows. The particle conservation equation is solved:

$$\frac{\partial n_{\mathrm{I}}}{\partial t} = -\nabla \cdot \Gamma + S_{\mathrm{I}} \tag{1}$$

where S_{I} is the sum of the particle source and sink terms. A common modelling assumption is to represent the flux Γ as a sum of two terms

$$\Gamma = -D\nabla n_{\mathrm{I}} + v n_{\mathrm{I}} = -D\frac{\partial n_{\mathrm{I}}}{\partial r} + v n_{\mathrm{I}} \tag{2}$$

where D is the radial diffusion coefficient and v is the radial convection, or 'pinch', velocity. The coefficients $D(r)$ and $v(r)$ provide a convenient way of describing a particular plasma transport regime. Surface averaged particle and heat fluxes Γ can be related to the thermodynamic forces $\{\nabla u\}_n$ in the matrix form $\Gamma = M\nabla u$. M represents a matrix of energy and particle transport coefficients, whereas u_n are particle temperature, density and toroidal electric field. Purely diffusive transport is represented by the diagonal D coefficient, whereas the off-diagonal matrix elements represent non-diffusive contributions, described by v. The

equations (1) and (2) are solved under the condition that impurity charge states are independent from the source: $S_I \simeq 0$ in the central region steady state plasma. This method yields the v/D ratio and under additional constrains D and v coefficients may also be estimated.

Other spectroscopic methods used in impurity transport measurements are charge exchange recombination spectroscopy [25] and passive vacuum ultraviolet spectroscopy of transiently introduced non-intrinsic impurities (e.g. [26]). Both methods are indisputably more accurate than the method used in this work. However, they require complex and expensive hardware and work only in plasma devices with plasma flat-top lifetimes of at least $0.1\,s$. Therefore, they would not be applicable to a small plasma device built for concept exploration. The utility of CDX-U spectroscopic diagnostic complex is that it measures radiated power and impurity brightness profiles of several impurity species simultaneously. The modelling matches the measurements for a narrow range of possible D and v coefficients. These D and v coefficients are not unique and not exact; however with the proper error analysis they can be compared to neoclassical theory predictions and other experiments. Such an approach is an inherent feature of concept exploration plasma experiments. Detailed measurements of local transport and underlying physics mechanisms can be accomplished on a larger facility with better diagnostic capabilities.

The structure of the paper is as follows. Section 2 discusses the CDX-U device and its plasma properties. Section 3 presents the interpretation of impurity measurements, numerical simulations of impurity profiles and neoclassical transport calculations. Section 4 discusses the results of the impurity transport measurements in CDX-U.

2. Experiment

A brief description of the CDX-U tokamak, its diagnostics, and the plasmas obtained in the 1999–2000 run campaign and used for impurity transport analysis are given in this section. Table 1 lists the parameters of CDX-U device. ohmic heating in CDX-U is achieved by consecutive discharging of two capacitor banks through a central solenoid, resulting in a plasma current ramp-up rate of 10–15 MA s^{-1}. Plasma discharge programming utilizes pre-programmed shaping coil current waveforms, and the proper timing between the ohmic heating coil current forms and the neutral gas fuelling from two gas injectors. Vertical and horizontal boron carbide rail limiters are used to prevent plasma–vacuum vessel interactions. The CDX-U diagnostics used in this work will be briefly discussed below, whereas a full diagnostic review can be found in [24]. Various profiles measured as a function of a major (R) or a minor (r/a) radii are transformed to one-dimensional functions of flux surface label with the dimensionality of a minor radius a.

Table 1. CDX-U parameters in 1999–2000 run campaign.

Major radius	R	0.35 m
Minor radius	a	0.22 m
Elongation	χ	$\leqslant$1.6
Nominal aspect ratio	A	1.5
Toroidal field	B_t	0.23 T
ohmic heating power	P_{OH}	300 kW
HHFW heating power	P_{HHFW}	100 kW
Plasma current	I_p	$\leqslant 7.5 \times 10^4$ A
Pulse duration	t_d	$\leqslant$0.02 s
Flat-top duration	t_{ft}	$\leqslant$0.005 s

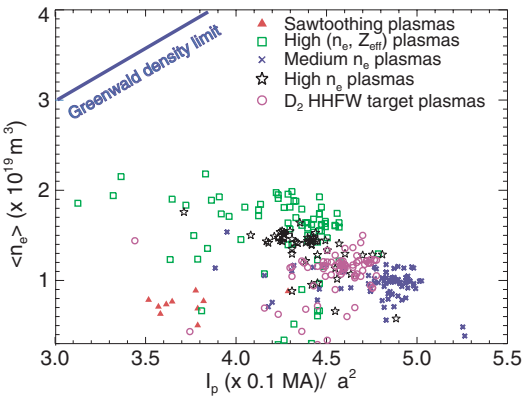

Figure 1. CDX-U plasma operational space in respect to the Greenwald limit, shown by the solid line.

The L-mode CDX-U plasmas are obtained by ohmic heating only. Average β in these plasmas is $\langle\beta\rangle = 2\mu_0\langle p\rangle/B^2 \leqslant 1\%$, where p is the average plasma pressure in Pa, and B is the magnetic field in T. Energy confinement time measurements are beyond the present diagnostic capabilities of CDX-U. The START energy confinement time scaling yields $\tau_{\rm E} \leqslant 1.4$ ms, whereas the neo-Alcator scaling yields $0.3 \leqslant \tau_{\rm E} \leqslant 0.5$ ms. Confinement in CDX-U is likely to be limited by the disruptive activity of MHD modes. The operational space of CDX-U plasmas is shown in figure 1. The electron density $\bar{n}_{\rm e} \simeq (0.2\text{–}0.5) \times n_{\rm G}$, where $n_{\rm G} = I_{\rm p}(\pi a^2)^{-1}$ is the Greenwald density [27]. The higher $\bar{n}_{\rm e}$ plasmas, which are not far from the Murakami disruption limit [28], are obtained by gas puffing throughout the discharge. The typical Murakami parameter $M = \bar{n}_{\rm e}R/B$ is between 0.1 and 0.2.

Electron temperature profiles in CDX-U are measured by the multipoint Thomson scattering system (TVTS) [29]. Typical profile measurements are shown in figure 2. Also shown are the edge $T_{\rm e}$ measurements taken by a Langmuir probe. Line integrated electron density $\int_{\rm L} n_{\rm e}\,{\rm d}l$ is measured by a movable one chord microwave interferometer [30]. A typical electron density profile $n_{\rm e}(r)$ (figure 2) is obtained by Abel inverting line integrated densities measured on a shot to shot basis at different radii. Both $T_{\rm e}$ and $n_{\rm e}$ profiles are highly peaked within $r/a \leqslant 0.4$, suggesting modest energy and particle confinement and a possibility of a transport barrier. The main plasma impurities are carbon and oxygen. Titanium gettering is used for impurity content reduction. The concentrations of carbon and oxygen varied through the 1999–2000 run campaign between 4–16% and 1–2% of electron density. The corresponding plasma effective charge, calculated from the impurity density measurements as described below, was $1.4 \leqslant Z_{\rm eff} \leqslant 2.5$. The plasmas with accidental titanium injections and high harmonic fast wave (HHFW) heated plasmas were characterized by higher effective charge $1.5 \leqslant Z_{\rm eff} \leqslant 3$ and higher radiated power $P_{\rm rad}$. Three multichannel spectrally filtered diode array diagnostics in combination with visible and VUV spectrometers and monochromators are used to obtain the core impurity emissivity profiles and a radiated power profile, as follows. The O VI profile is recorded with $\tau \simeq 40\,\mu$s temporal resolution using a ten channel multilayer mirror (MLM) absolute extreme ultraviolet (AXUV) diode array [31]. Each channel is a miniature XUV monochromator tuned to the 2s–2p transition of lithium-like oxygen at $\lambda = 150$ Å. Radiated power profiles are measured by a ten channel AXUV diode array [31] operated in the radiometric mode. This array is also equipped with interchangeable

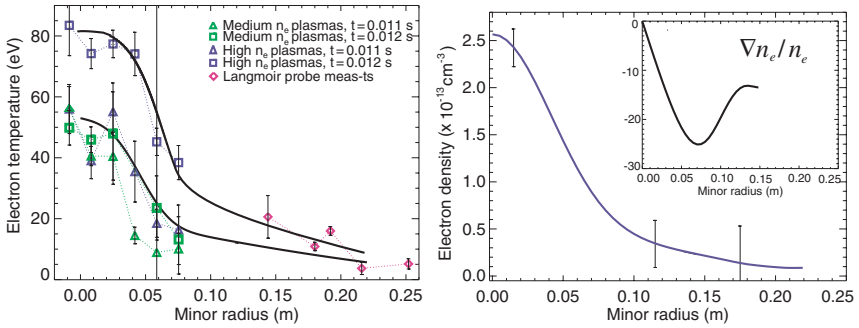

Figure 2. Electron temperature and density profiles in a typical CDX-U discharge. Solid lines show idealized profiles.

beryllium and titanium filters which allowed the transfer of its absolute calibration to the surface barrier diode (SBD) array. The thirty channel SBD array [32] is used for soft x-ray (SXR) profile measurements. This array is also equipped with Be and Ti foil filters. An XUV grazing incidence spectrometer STRS [33] upgraded with a charge coupled device (CCD) detector is used to identify the lines within the SBD array filter bandpass. For the described discharge conditions the beryllium filter transmits predominantly O V and O VI line radiation, whereas C V λ41 2s–2p transition by far dominates the signal obtained with the titanium filter [31]. Emissions from the lower charge states of oxygen and carbon are monitored by a 0.5 m McPherson visible monochromator and a novel design vacuum ultraviolet monochromator [34]. The latter instrument was constructed for impurity measurements in a tokamak divertor. It measures the C IV λ1550 brightness along a midplane line of sight with a chordal radius of $R = 0.3$ m. The Doppler broadening of the C III λ4650 triplet lines is used for impurity ion temperature estimate. The measurements are performed with a 1 m McPherson 2061 monochromator and a CCD camera detector. The neutral density profile $n_{\mathrm{D}}(r)$ is estimated from the H_α-filtered plasma images.

3. Analysis

3.1. Plasma conditions in impurity transport experiments

Shown in figure 3 are the waveforms of a representative hydrogen discharge. The baseline plasma conditions are characterized by I_{p}, V_{loop}, $\bar{n}_{\mathrm{e}}$; the T_{e} and n_{e} profiles; edge T_{e} and n_{e} Langmuir probe measurements; and extensive spectroscopic coverage of impurity emission. Both MHD quiescent and MHD dominated discharges have been obtained. A typical value of cylindrical equivalent of the safety factor is $q_{\mathrm{cyl}} \simeq 2$, and an estimated $q_a \leqslant 7$. The $n/m = 1/1, 1/2$ modes develop typically in the end of flat-top at $t = 12$–13 ms. The $q = 1$ surface radius inferred from the $n/m = 1/1$ island position is 5–7 cm. Several reconnection events (REs) are frequently observed prior to discharge termination. A summary of MHD observations is given in appendix B. The carbon and oxygen concentrations in these plasmas are $c \simeq 1$–2% of electron density. The time traces of C III/C IV, C IV/C V and O II/O VI in the flat-top phase are characteristic of a constant rate of impurity influx into the plasma. Central radiated power density is 25–35 mW cm^{-3}. This radiated power density corresponds to the total radiated power of about 5–10% of the total ohmic input power. The reason for the $P_{\mathrm{rad}}/P_{\mathrm{OH}}$

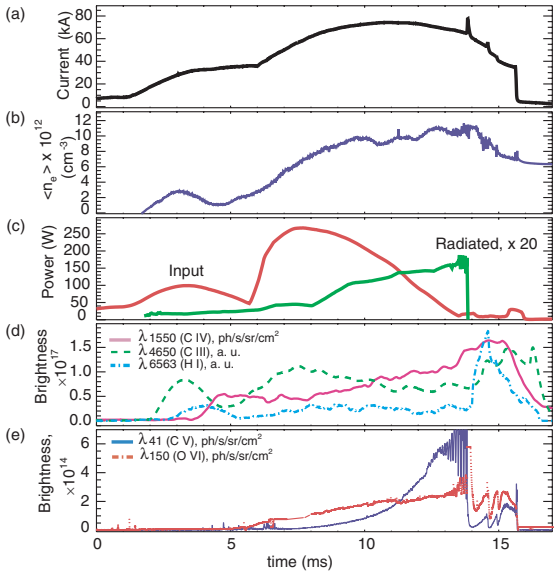

Figure 3. Time traces of plasma current I_p (*a*), $\bar{n}_e(0)$ (*b*), ohmic input and radiated power (*c*), edge and core impurity brightness ((*d*), (*e*)) in a typical hydrogen discharge.

being low is that the current channel in CDX-U is fairly narrow. As a result of peaked n_e and T_e profiles the power radiating region is limited to the very core, even though the plasma extends over the full vacuum vessel volume. The Z_{eff} profiles inferred from core impurity measurements are weakly peaked with $Z_{eff}(0)$ in the range between 1.5 and 2.2 .

3.2. Numerical modelling of impurity transport

Emissivity profiles are obtained by inverting the measured line integrated brightnesses [31] and modelled using the time dependent impurity transport code MIST [35,36] in combination with a new collisional-radiative package CRMLIN, briefly discussed in appendix A. Emissivity profiles of plasma P_{rad}, C V ($\epsilon_{\lambda 41}$), O VI ($\epsilon_{\lambda 150}$) and line integrated brightness of C IV ($B_{\lambda 1550}$) are modelled self-consistently. MIST solves a one-dimensional time-dependent radial continuity equation for impurity particles (equation (1)). Input are the plasma profiles $n_e(r,t)$, $T_e(r,t)$, $n_D(r,t)$, and the impurity source rate. Impurity flux Γ_I is parameterized as in equation (2). The convection velocity v is expressed in terms of the diffusion coefficient D and the peaking parameter C_{vne} [36]:

$$v(r) = C_{vne}\frac{\partial \ln n_e(r)}{\partial r}D \tag{3}$$

The obtained impurity density profile n_I is related to the n_e profile so that for $C_{vne} = 1$ the impurity density profile is as peaked as $n_e(r)$, whereas for $C_{vne} > 1$ the impurity density profile is more peaked than the n_e profile. The peak radial positions and the width of impurity ion density profiles are primarily determined by the absolute value of the diffusion coefficient D. The impurity density peaking factor and, to a lesser extent the peak radial position, are determined by convection velocity v. Time-dependent calculations are necessary

to model the impurity profile evolution since the flat-top duration of I_p, n_e, n_I is on the order of impurity confinement time. The scrape-off layer (SOL) parallel confinement time $\tau_\parallel = \lambda_{SOL} D^{-1} \leqslant 1.5$ ms, where λ_{SOL} is the SOL scale length. Neutral impurity source, D and v are chosen so that the measured and modelled O VI, C V, P_{rad} profiles and C III, C IV, and O II time histories match. The emissivities are taken from the emissivity tables calculated by CRMLIN as described in appendix A. Impurity densities are thus inferred from the iterative modelling.

The measurements from four spectroscopic diagnostics provide a rigid constraint on modelling. At $T_e \leqslant 80$ eV O VI and C V profiles alone would not provide an adequate constraint. Both profiles are peaked, sensitive to the C_{vne} value which determines their peaking factor, however much less sensitive to the D value. The O VI and C V profiles become more sensitive to D at $T_e \geqslant 100$ eV when both charge states are partially 'burned through'. Thus, an additional constraint is provided by the radiometrically calibrated C IV monitor and radiometer array signals. The λ1550 C IV brightness time history provides a measure of carbon edge influx. The radiated power density profile constrains impurity charge state emission shell locations. If too large of a D is used in simulations, the peripheral charge states, namely C III, O IV, O V, and partly C IV, are spread between $r/a = 0.35$ and $r/a = 0.8$. This significantly broadens the P_{rad} profile. Shown in figure 4 is the parameter space of the diffusion and convection coefficients. When $0.2 \leqslant D \leqslant 0.6\,m^2\,s^{-1}$ and $0.3 \leqslant C_{vne} \leqslant 1.5$ are used, the simulated profiles match the experiment. It is important to emphasize that the modelling of C V, O VI, and plasma emissivity profiles is sensitive not only to $T_e(r)$ and $n_e(r)$ but also to the transport coefficients D and v. Thus, the peaked profiles can be modelled only with a low radially constant diffusion and a large inward pinch. Figure 5 demonstrates these arguments: the measured profiles in a medium $\bar{n}_e \simeq 0.2 \times n_G$ hydrogen discharge are compared to the modelled profiles with $D = 0.4\,m^2\,s^{-1}$ and $0.1 \leqslant C_{vne} \leqslant 1.5$. Similar results were obtained for the plasmas with $\bar{n}_e \simeq 0.5 \times n_G$. Shown in figure 6 are the modelled carbon and oxygen charge state distributions. The C V density is peaked, C IV is distributed evenly within $0 \leqslant r/a \leqslant 0.1$, and C III is in the periphery, which is in good agreement with the measurements. The O VI density is peaked and O II peaks at the extreme edge, as expected. The range of values of D and v inferred from the modelling, although mathematically not unique, gives an insight into the transport problem and can be compared with theoretical predictions. A constant diffusion coefficient $D = 0.4 \pm 0.2\,m^2\,s^{-1}$ was used in the modelling for simplicity, since the present

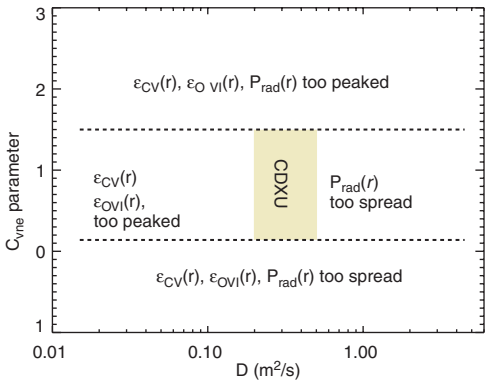

Figure 4. Modelled transport parameters D and C_{vne} that match the measurements (shaded area), and the modelling criteria.

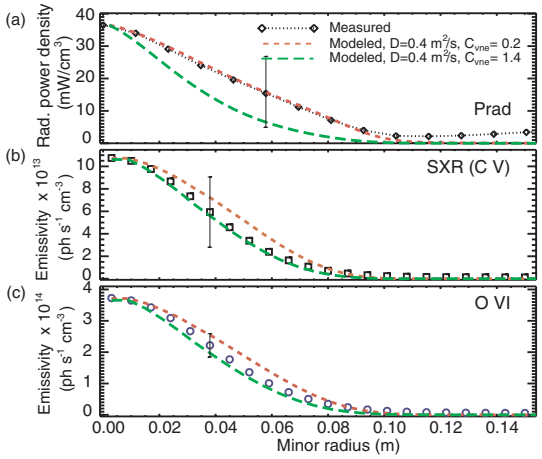

Figure 5. Comparison of modelled and measured profiles: (*a*) radiated power, normalized to measured signal, (*b*) C v absolute brightness profile, (*c*) O vi absolute brightness profile.

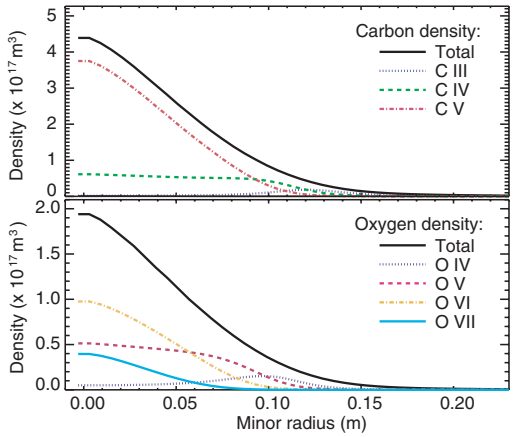

Figure 6. Modelled carbon and oxygen charge state distributions.

analysis can only yield global transport coefficients. An alternate solution with a discontinuity of $D(r)$ is briefly discussed in section 4. The convective velocity inferred from the modelling is $2 \leqslant v \leqslant 20\,\mathrm{m\,s^{-1}}$ and is directed inward. The range of parameter $0.1 \leqslant C_{\mathrm{vne}} \leqslant 1.5$ implies that the impurity profiles peaked both slightly more and slightly less than $n_{\mathrm{e}}(r)$ match the experiment. Finally, the inferred diffusion is $D \simeq (0.02\text{–}0.05) \times D_{\mathrm{Bohm}}$, where the Bohm diffusion is $D_{\mathrm{Bohm}} = 10^4 \times T_{\mathrm{e}} \times (16 B_t)^{-1}$, and T_{e} is in eV, B is in Gauss, and D_{Bohm} is in $\mathrm{cm^2\,s^{-1}}$.

3.3. Neoclassical theory predictions

Standard neoclassical theory of particle and heat transport [13, 14, 37] is based on the solution of multi-species moment equations that follow from the Vlasov Fokker–Plank equation.

A particle distribution function expansion in terms of powers of the inverse aspect ratio ϵ is used in the solution of the equations and derivation of particle fluxes and transport coefficients. The theory has been successful in explaining impurity measurements in large aspect ratio circular tokamaks [15, 38, 39]. However, for small aspect ratio tokamaks ϵ is no longer a small parameter. The second complication is that the toroidal field in low aspect ratio tokamaks is low, and as a result particle gyro-radii are large. In CDX-U the electron gyro-radii is $\rho_e \simeq 0.1$ mm, ion gyro-radius is $\rho_i \simeq 3$ mm, and the highly ionized impurity gyro-radius is $\rho_I \simeq 20$ mm. Particle fluxes are derived in [14] under the assumption $\rho/L_n \ll 1$, where L_n is the radial scale length of density and temperature. This condition is not satisfied in CDX-U. Therefore, the standard analytical neoclassical theory predictions are likely to be misleading for the small aspect ratio geometry and the peaked CDX-U profiles, in particular. Recently derived analytical expressions for plasma viscosity [40, 41] are implemented in the neoclassical codes NCLASS and FORCEBAL [42] and avoid these shortcomings. The FORCEBAL code is used in this work to estimate the neoclassical impurity fluxes and transport coefficients. Input are the measured temperature and density profiles. A magnetic equilibrium consistent with poloidal cross-section SXR and radial bolometry profiles is used. Carbon and oxygen are found to be in the collisional, or Pfirsch–Schluter (PS) regime, from the intermediate to the extreme range: $0.8 \leqslant \nu_* \epsilon^{3/2} \leqslant 3$. Working ions are in the Banana–Plateau (BP) regime: $0.08 \leqslant \nu_* \epsilon^{3/2} \leqslant 1$. Here, $\nu_* \epsilon^{3/2}$ is the commonly used collisionality parameter [14]. FORCEBAL calculations include the classical, BP and PS fluxes simultaneously, and the transition between the collisionality regimes is treated as a continuous function. Neoclassical impurity fluxes and transport coefficients are calculated in the reduced charge state approximation. The impurity strength parameters $\alpha_I = n_I Z_I^2 / n_i Z_i^2$ for carbon and oxygen in the region of interest $r \leqslant 0.1$ m are $0.15 \leqslant \alpha_C \leqslant 0.3$ and $0.2 \leqslant \alpha_O \leqslant 0.5$. Hence, both carbon and oxygen are 'strong' impurities and the collisional friction forces R_{ab} are dominated by ion-impurity interaction since $R_{ei}/R_{iI} \sim \sqrt{m_e/m_i}/\alpha_I$ [14]. The masses, average charge distribution and collisionalities of carbon and oxygen are close: thus, to first approximation carbon and oxygen may be treated as one low-Z impurity. Two types of neoclassical calculations have been performed. The first type includes only the friction between one low-Z impurity and the ions. Total carbon and oxygen impurity densities, average impurity charges and Z_{eff} profiles obtained from the MIST modelling are used. Figure 7 compares the calculated neoclassical diffusion coefficient and the convection velocity with the ones derived from MIST modelling. In the $r/a < 0.4$ region the experimentally inferred diffusion is at the neoclassical level, whereas the convection velocity is within a factor of 2–3 smaller than the neoclassical one. The dominant contribution, about 70%, to the total neoclassical impurity flux comes from the PS flux. The second type of calculation includes both carbon and oxygen impurities, and the friction between each other and the working ions. The introduction of the second impurity changes the calculated D and v for the first impurity very little. This suggests that self-friction of the low-Z impurity is negligible. The D_{neo} and v_{neo} radial profile shape is sensitive to the $T_{e,i}(r)$ and $n_{e,i}(r)$. Variations of these profiles within the experiment errors, as well as the scaling of $T_i(r)$ from $0.5 \times T_e$ to T_e, produce the range of D_{neo} and v_{neo} shown in figure 7 by shaded forms. It is worthwhile to mention the working ion and electron transport parameters predicted by FORCEBAL: $D_i \simeq 0.03$–$0.1\ m^2\ s^{-1}$, $v_i \simeq 2$–$3\ m\ s^{-1}$, $D_e \simeq 0.01$–$0.02\ m^2\ s^{-1}$, $v_e \simeq 0.1\ m\ s^{-1}$, and $\chi_e \simeq 0.03$–$0.05\ m^2\ s^{-1}$.

Finally, shown in figure 8 are the v/D ratios obtained from the measured profiles and neoclassical calculations. The neoclassical v/D ratio is about a factor of four greater than the v/D ratios inferred from the MIST modelling (v_{MIST}/D_{MIST}) and from the measured profiles ($v_{meas}/D_{meas} = \nabla n_{C,O}/n_{C,O}$). The discrepancy is mainly due to $v_{meas}/v_{neo} < 1$. The impurity density $n_{C,O}$ is directly inferred from $n_{C,O}(r) = \epsilon_{exp}(r) n_e^{-1} P^{-1}(T_e, n_e)$, where $\epsilon_{exp}(r)$ is the

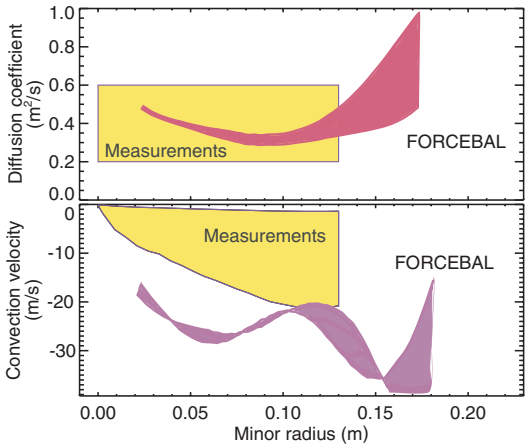

Figure 7. Neoclassical D and v profiles calculated using FORCEBAL. The range of D and v inferred from the measurements is shown by filled polygons.

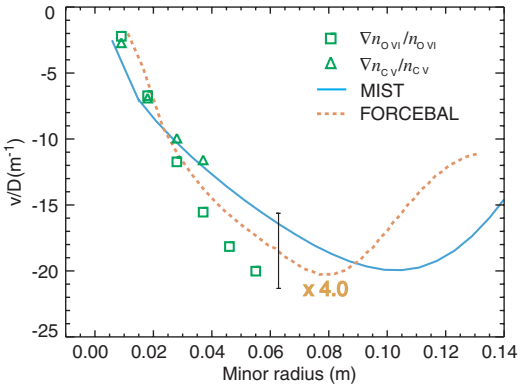

Figure 8. The ratio v/D inferred from measurements and modelling.

measured impurity emissivity in the units of photons s^{-1} cm^{-3} and $P(T_e, n_e)$ is the emissivity coefficient calculated using CRMLIN, as discussed in appendix A.

4. Discussion and conclusions

Two main results follow from the experiment and the modelling described in previous sections. First, impurity diffusion and convection velocity inferred from impurity profile measurements are close to the neoclassical ones. Second, the measured impurity profiles imply strongly non-diffusive transport: large inward pinch is required to explain peaked carbon and oxygen profiles. The section discusses these results in detail.

Both the neoclassical and anomalous transport mechanisms may simultaneously contribute to the formation of radial particle and heat profiles [38]:

$$\Gamma_{\rm tot}(r) = \Gamma_{\rm neo}(r) + \Gamma_{\rm anom}(r) = -(D_{\rm neo} + D_{\rm anom})\nabla n_{\rm I} + (v_{\rm neo} + v_{\rm anom})n_{\rm I} \qquad (4)$$

where $\Gamma_{\rm neo}(r)$, $\Gamma_{\rm anom}(r)$ are the neoclassical and anomalous radial particle fluxes, respectively. In CDX-U plasmas $\Gamma_{\rm neo}$ is dominant in the region $r/a \leqslant 0.4$ suggesting that $D_{\rm anom} \simeq 0$ and core turbulence is reduced.

Regardless of the collisionality regime, the neoclassical impurity flux can be written as [39]

$$\Gamma_{\rm I} = -D\nabla n_{\rm I} + vn_{\rm I} = -D^{\rm neo}\nabla n_{\rm I} + D^{\rm neo}\left(\left(\sum_{j\neq I} g_{n_{jI}}\frac{\nabla n_j}{n_j}\right) + g_{T_{\rm i}}\frac{\nabla T_{\rm i}}{T_{\rm i}}\right)n_{\rm I} \qquad (5)$$

where $g_{n_{jI}}$ and $g_{T_{\rm i}}$ depend on collisionality, aspect ratio, and plasma profiles of species j, ions (i), and electrons (e). The described CDX-U plasma is an interesting case in the following way: electrons and ions in CDX-U are in the BP regime, whereas low-Z impurities are in the collisional regime. Particle density and temperature peaking factors and gradients are large. The low toroidal field $B_{\rm t} \sim 0.2\,{\rm T}$ results in large particle gyro-radii: $\rho_{\rm L} \leqslant 1\,{\rm cm}$. These quantities directly enter the neoclassical impurity transport expressions. If the anomalous transport is reduced, then particle transport is determined by the particle density and temperature gradient driven forces. The classical flux is due to the radial friction (momentum exchange) between impurities and ions, and is important near the plasma centre. The BP flux is driven by pressure anisotropy associated with viscous forces, and is important for low collisionality. At high collisionality, pressure anisotropies become small, and the flux is mainly due to the poloidal variation of the parallel friction forces (the PS flux). As noted in section 3.3, impurity self-friction appears to play a minor role. The ion-impurity friction force drives the impurities toward the peak of the ion density distribution and includes contributions from both density and temperature gradients. The degree of $T_{\rm i}$ peaking becomes important only when the $n_{\rm i}$ gradient is small. The temperature gradient term is responsible for the temperature screening effect: the thermal force acts on the impurities in the direction of the thermal gradient and prevents them from penetration into the plasma core. The temperature screening effect has been observed in several tokamak experiments [39, 43]. An interesting consequence of this effect is that in a stationary transport regime, its failure can result in an impurity accumulation instability. The impurity accumulation instability model was proposed to explain high-Z impurity accumulation in several tokamaks [43–45]. The model assumes that (i) the transport is neoclassical, with low D and large v, (ii) the high-Z impurities are in the Pfirsch–Schluter regime, (iii) radiative loss in the plasma core due to impurities is a large fraction of the input ohmic power. Simultaneous achievement of these conditions can lead to the following scenario. The central ion temperature decreases due to radiative cooling of the core, the temperature gradient decreases thus diminishing the strength of the temperature screening effect. This causes the impurity inward flux to increase. The enhanced core power loss due to increased impurity radiation leads to further ion temperature decrease and further temperature screening effect failure. The instability threshold is defined in terms of the critical electron density $n_{\rm e}(0)$: $n_{\rm I}(0)/n_{\rm e}(0) \sim 4\times10^{-2}\times(D_\perp/D_{\rm neo}^{\rm PS})^2$ [43]. Observations in CDX-U plasmas prior to 1999 appeared to satisfy the criteria of the accumulation instability for low-Z impurities [46]. Infrequent auxiliary plasma heating observed in the HHFW experiments prior to 1999 also seemed to corroborate the instability model [46]. However, the model failed to explain the 1999–2000 run campaign measurements. The measured radiated power is only a small fraction of the input power: $P_{\rm rad}^{\rm max} \sim 0.2P_{\rm ohmic}^{\rm in}$. Therefore, the change in $P_{\rm rad}$ would not cause any significant electron or ion cooling. The peaked $n_{\rm i}$ profile has a much larger effect on impurity distribution in the collisional regime because the contribution from

$\nabla n_i/n_i$ terms is larger than the contributions from $\nabla T_i/T_i$ terms. Persistent highly peaked ion density profiles appear to be the main reason for the peaked impurity profiles. Comparison of figures 2 and 7 shows that the neoclassical $v(r)$ profile closely follows $\nabla n_i/n_i$. The n_i profile is obtained from the n_e and Z_{eff} profiles. Because $Z_{eff}(r)$ is only slightly peaked, $\nabla n_i/n_i$ and $\nabla n_e/n_e$ are very similar. It is interesting to note that highly peaked ion profiles in conventional tokamaks typically arise due to central fuelling, such as pellet or neutral beam injection and do lead to neoclassical impurity peaking (e.g. [47, 48]).

The shape of measured T_e and n_e, namely a peaked part and a 'plateau' part, suggests that a particle transport barrier may exist at $r/a \simeq 0.35$–0.45. A constant D was used to simplify the numerical impurity simulations and because of the lack of reliable measurements in the region outside $r/a \geqslant 0.4$. The particle diffusion coefficient may not be radially constant in CDX-U: a discontinuity in D could also explain the highly peaked electron, ion, and impurity profiles. MIST simulations have been performed with the step-like $0.4 \leqslant D \leqslant 1.0\,\mathrm{m^2\,s^{-1}}$ with the step located at $r/a \simeq 0.35$–0.45. The simulated profiles came within about 50% with the experimentally measured profiles. This conjecture does not change the results of present work, however may help interpret future CDX-U results.

As noted, the length of CDX-U pulse is mainly limited by the available ohmic transformer flux, and by the MHD disruptive activity. Present CDX-U discharges are too short to observe the possible transport-related impurity accumulation effects that may lead to radiative cooling of the core and plasma thermal collapse. A rough impurity confinement time estimate based on the inferred diffusion is about 50 ms and is much greater than the present length of CDX-U discharge.

Finally, it is of interest to compare the results of this work with other impurity transport measurements in ohmically heated plasmas of small and medium size, moderate current, large aspect ratio tokamaks TEXT, TFR, TEXTOR, TdeV ([49] and references therein) and Phaedrus-T [50]. Core steady-state impurity transport in these experiments has been found to be anomalous, based on $D_{measured} \gg D_{neo}$. In contrast, we find that $D_{measured} \simeq D_{neo}$ and $v_{measured} \leqslant v_{neo}$ in CDX-U. This suggests that drift-wave microinstabilities are suppressed in the core of CDX-U, since the collisional transport is smaller in magnitude than the transport induced by turbulence. The lack of turbulence measurements precludes us from discussing this subject further. It is also unclear whether the obtained results can be generalized to ohmic or L-mode plasmas obtained in larger STs.

In summary, carbon, oxygen, and radiated power profiles have been measured in ohmically heated hydrogen plasmas of CDX-U low aspect ratio tokamak using state of the art VUV spectroscopy techniques. The inferred steady-state impurity density profiles imply strongly non-diffusive transport: large inward pinch is necessary to explain the measurements. Impurity transport coefficients have been derived using numerical solution of radial continuity equations for all carbon and oxygen charge states constrained by the measurements. The inferred diffusion coefficient is $0.2 \leqslant D \leqslant 0.6\,\mathrm{m^2\,s^{-1}}$, and the convective velocity is $v \simeq 4$–$16\,\mathrm{m\,s^{-1}}$. These transport coefficients are close to the predictions by the FORCEBAL code using neoclassical theory expressions valid for an arbitrary aspect ratio geometry and collisionality. Following the neoclassical analysis, the ion density gradient term is identified to be the main factor for impurity density peaking in CDX-U.

Acknowledgments

We would like to thank Mr J Taylor (PPPL) for technical support. Dr W Houlberg (Oak Ridge National Laboratory) is acknowledged for the code FORCEBAL. This work was supported by the US Department of Energy Grant DE-FG02-86ER53214 at the Johns Hopkins University and

the US Department of Energy Contract DE-AC02-76-CH03073 at Princeton Plasma Physics Laboratory.

Appendix A. Atomic data and collisional-radiative calculations

This appendix summarizes the atomic data sources and collisional-radiative calculations used in interpretation of CDX-U spectroscopic measurements. The full $n \leqslant 4$ collisional-radiative model (CRM) calculations were performed by the CRMLIN suite of codes. Emissivities for carbon and oxygen lines of interest P_λ are calculated and stored in a tabular form as $P(T_e, n_e) = A_{ij}\, n_j(T_e, n_e)\, n_I^{-1} n_e^{-1}$, where A_{ij} is the probability of the radiative transition from level j to level i, and the (occupancy number) of the level n_j is obtained by solving the CRM steady-state coupled rate equations.

Carbon. The LS-resolved C II, C III, C IV, C V, and C VI data used in this work are from the astrophysical database CHIANTI [51, 52]. CHIANTI is a compilation of the best available published atomic data for astrophysically abundant elements. Multiplet-unresolved energy levels and electron collision strengths for C I are taken from [53]. C I oscillator strengths, transition probabilities and wavelengths are from [54]. Multiplet-unresolved energy levels, wavelengths and electron excitation rates for C V and C VI ions from ALADDIN [55] have been used in radiated power calculations.

Oxygen. Atomic data for O II, O III, O IV, O V, and O VI are taken from the CHIANTI database. O VII and O VIII energy levels, wavelengths and electron excitation rates are from ALADDIN [55]. O VI λ150 emissivity calculated using the data from CHIANTI was found to be systematically 25% higher than the emissivity obtained with ALADDIN data. This is attributed to the higher accuracy O VI collision strengths, calculated in the relativistic distorted wave approximation [56].

Ionization and recombination rates. Total ionization and recombination rates used in MIST calculations are as follows: the carbon and oxygen ionization rates are from [57] and the recombination rates are from semi-empirical formula calculations (e.g. the Burgess-Mertz formula for dielectronic recombination rate [58, 59]). The MIST version with the most recent ionization and recombination rate compilation from [60, 61] was also available [62]. For low-Z impurities, the densities calculated by MIST using the semi-empirical and best available rates are well within the uncertainty of the experiment.

Appendix B. MHD activity observations

MHD properties of CDX-U plasmas are summarized in this section. Almost all types of CDX-U discharges show some MHD activity, namely the low n/m modes, sawtooth instabilities, and reconnection events. Recent theoretical calculations [63] and the experimental results from the START spherical torus [10] demonstrate the enhanced stability of the small aspect ratio high β toroidal configuration against ideal ballooning and kink modes.

Low n/m modes. The 1/1 and 1/2 modes, or 'snakes' [64], are observed spectroscopically with the SXR arrays. The instability is likely to be either a tearing mode or a kink mode. The rotation frequency of the $n/m = 1/1$ island is 11–12 kHz (period $\tau_{1/1} \simeq 80\,\mu$s), and approximately twice this value for the $n/m = 1/2$ mode. The $n/m = 1/2$ mode is usually locked in phase with the $n/m = 1/1$ mode. The width of the observed 1/1 island is several centimetres, and

the radial position of the island, corresponding to the $q = 1$ surface, is typically between 5 and 10 cm. An accumulation of impurity ions inside the $n/m = 1/1$ island is frequently observed. Carbon density inside the island frequently exceeds the local density at the rational $q = 1$ surface, up to a factor of three. The accumulation results from the short-circuiting of the local parallel and perpendicular particle transport between the X points of the magnetic island. To avoid measurement uncertainties and possible transport implications resulting from the rotating magnetic islands, all impurity profiles for the transport measurements have been evaluated before the onset of the MHD activity.

Sawtooth instability. The sawtooth oscillations in CDX-U are observed rarely, in fact only several ohmic and HHFW heated shots displayed the sawtooth activity. The current ramp-up rate of the OH1 (the ohmic coil fed by the first capacitor bank) in these discharges was almost twice as high as in a typical CDX-U discharge, and apparently the central $q(0)$ quickly approached unity. For the onset of sawtooth oscillation the q profile must be sufficiently shaped, so that $q(0)$ is close to unity and $q(a)$ is large enough to create a peaked current profile. MHD mode activity may be one of the reasons that an adequate current profile is rarely obtained. Another reason may be the influence of the peaked impurity profiles on plasma conductivity [48]. A peaked $Z_{\rm eff}$ profile may lead to a flat or even hollow conductivity profile. This would result in flattening (or hollowing) the current profile and the safety factor $q > 1$ everywhere, which in turn would suppress the sawteeth. The $q = 1$ surface radius is $r_{q=1} \simeq 3.5$ cm, and the inversion radius is $3 \leqslant r_{\rm inv} \leqslant 5$ cm. The sawtooth amplitude is $0.2 \leqslant A \leqslant 0.4$, defined as $A = \Delta S/\max(S)$, where S is the amplitude of the SXR signal.

An estimate of $\Delta T_{\rm e}$ in the sawtooth crash has been made using the following argument [65]. Shown in figure 9 are the SXR profiles measured immediately before and after the sawtooth crash and averaged over five sawtooth periods. The brightness difference is Abel inverted and the emissivity difference profile $\Delta E(r)$ is obtained. The quantity E is related to the λ41 C v emissivity $\varepsilon_{\lambda 41}$, expressed in the units of photons $\mathrm{s}^{-1}\, n_{\rm e}^{-1}\, n_{\rm C\,V}^{-1}$ through: $E(r) = n_{\rm e} n_{\rm C\,V} \varepsilon_{\lambda 41}(T_{\rm e})$. The difference in the emissivity for the times proceeding and following the sawtooth crash can be expressed as:

$$\Delta E(r) = (n_{\rm e} + \Delta n_{\rm e}) n_{\rm C\,V} \varepsilon_{\lambda 41}(T_{\rm e} + \Delta T_{\rm e}) - n_{\rm e} n_{\rm C\,V} \varepsilon_{\lambda 41}(T_{\rm e}) \tag{B.1}$$

The line averaged density $\bar{n}_{\rm e}(t)$ in the sawtooth phase is practically unchanged; thus $\Delta n_{\rm e}$ can be neglected. An estimate of $\Delta T_{\rm e}$ based on measured $\Delta E(r)$ and calculated $\varepsilon_{\lambda 41}$ follows. The

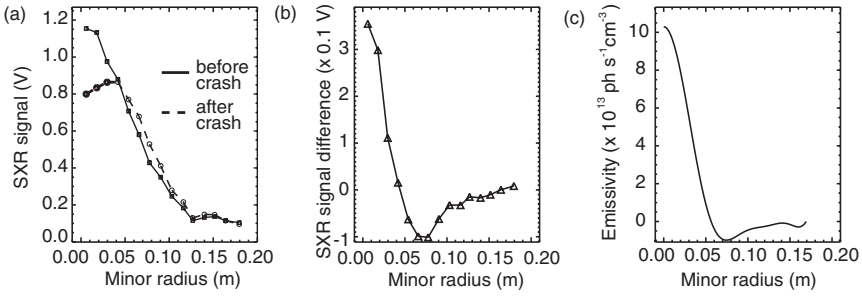

Figure 9. (*a*) SXR brightness signals before and after the sawtooth crash averaged over five sawtooth periods. (*b*) Difference of the brightness signals. (*c*) Abel inverted emissivity difference.

temperature difference is $\Delta T_e = 20$–$30\,\mathrm{eV}$, and the estimated central electron temperature is $T_e \simeq 80\,\mathrm{eV}$. The central electron density in these discharges is $n_e(0) \simeq 1.8 \times 10^{13}\,\mathrm{cm}^{-3}$, and the C V concentration was estimated to be 4–6%. The electron temperature difference of 20 to 30 eV yields the sawtooth reheat rate of $\gamma = \Delta T_e/(\tau_{ST} - \tau_{crash}) \simeq 75\,\mathrm{keV\,s}^{-1}$. This value is comparable to the sawtooth reheat rates measured in large tokamaks [66]. The measured sawtooth crash time is $\tau_{crash} \simeq 30$–$50\,\mu\mathrm{s}$, and the period is $\tau_{ST} \simeq 320$–$400\,\mu\mathrm{s}$. The estimated Kadomtsev crash time is $\tau_{crash} \simeq 40\,\mu\mathrm{s}$. The sawtooth period τ_{ST} depends on several parameters: the resistive time scale τ_R, the current profile and the magnitude of the neoclassical part of the resistivity profile $\eta(r)$. Several sawtooth period scaling laws have been developed based on the observations from many tokamak experiments. The scaling proposed in [67] has the form $\tau_{ST} \sim \tau_R/\epsilon_s^2 \simeq 9R^2T_e^{3/2}/Z_{eff}$ where τ_{ST} is in ms, the major radius R is in m, T_e is in keV, and ϵ_s is the inverse aspect ratio $\epsilon = r_s/R$. For CDX-U parameters the scaling yields $\tau_{ST} \simeq 20\,\mu\mathrm{s}$. This is an order of magnitude smaller than the observed τ_{ST}. The scaling [68] derived for small ohmic tokamaks has the form $\tau_{ST} \simeq 3\tau_R^{3/7}\tau_A^{2/7}\tau_H^{2/7}$ where all τs are in ms and τ_H is the heating time $\tau_H = 3n_eT_e/2\eta j^2$, j being the central current density. This scaling gives $\tau_{ST} \simeq 180\,\mu\mathrm{s}$ for CDX-U, twice the measured τ_{ST}, suggesting that the sawtooth oscillation properties are similar for small ohmic plasmas regardless of the aspect ratio.

In contrast with many observations from conventional tokamaks [69–71], the sawtooth oscillations in CDX-U do not perturb the impurity profiles to such a degree that a change in transport is necessary to explain the change in the profiles. The mixing radius r_{mix} is approximately one third of the impurity distribution radius. MIST simulations with periodically flattened temperature profiles over r_{mix} demonstrate that the $\Delta T_e \simeq 20$–$30\,\mathrm{eV}$ temperature change would be sufficient to explain the change in SXR and O VI emissivity profiles.

Reconnection events. The reconnection event (RE) is a global energy relaxation instability. It is principally different from the sawtooth oscillations in that its occurrence is not periodic and that the change in the magnetic topology and the resulting energy transfer affect the whole plasma volume. However, unlike the disruption instability in the large aspect ratio tokamaks, the plasma current and pressure are not terminated after the RE. After the RE occurs, the energy from the core is transported outwards, and the plasma pressure profile partially collapses. The RE was observed for the first time in the CDX-U and START spherical tori [10, 21], and termed the 'internal reconnection event'. Both 'internal' and 'global' reconnection events have been observed in CDX-U. The former typically affects the plasma within $r/a \leqslant 0.4$, whereas the latter occurs across $r/a \leqslant 0.8$. The phenomenological signs of the RE are the following. The current time trace demonstrates a positive spike up to 15% of the measured current. The RE is also accompanied by a loop voltage negative spike (ohmic current waveforms in CDX-U are pre-programmed and not fed-back), and enhanced limiter current activity, indicative of plasma-wall interaction. Some RE's do not produce the spike on the I_p and V_{loop} time traces. The total radiated power typically undergoes an instantaneous decrease as well, as the highly ionized impurities are thrown out of the central region to the periphery. The particle inventory undergoes a decrease; however in many cases it has recovered to pre-RE levels [31, 34]. The occurrence of the RE in CDX-U is correlated with several factors. The RE occurs only when the plasma loop voltage reaches a low value, typically below 1.5 V. The RE also occurs more frequently in the plasmas with higher density and higher Z_{eff}, making it phenomenologically close to major disruptions in large aspect ratio tokamaks. A possible cause of the RE is the MHD mode disruptive activity. The $n/m = 1/1, 1/2$ and higher m modes are frequently detected in CDX-U by magnetic and spectroscopic diagnostics directly preceding the RE.

Several theoretical and numerical models, attempting to explain the phenomenology of the RE, have emerged recently [72–74].

References

[1] Peng M 1998 *J. Fusion Energy* **17** 45
[2] Peng Y-K M and Strickler D J 1986 *Nucl. Fusion* **26** 769
[3] Gryaznevich M *et al* 1998 *Phys. Rev. Lett.* **80** 3972
[4] Gates D 2001 *IEEE International Conf. Plasma Science* O5E1
[5] Morris A *et al* 1999 *Plasma Phys. Control. Fusion* **41** B191
[6] Carter M D, Ryan P M and Swain D W 1998 *Fusion Technol.* **34** 407
[7] Jaeger E *et al* 1998 *Nucl. Fusion* **38** 1
[8] Raman R *et al* 2001 *Plasma Phys. Control. Fusion* **43** 305
[9] Raman R *et al* 2001 *Nucl. Fusion* **41** 1081
[10] Hender T C *et al* 1999 *Phys. Plasmas* **6** 1958
[11] Sabbagh S *et al* 1997 *Nucl. Fusion* **41** 1601
[12] Fredrickson E *et al* 2001 *Phys. Rev. Lett.* **87** 145001/1
[13] Hinton F L and Hazeltine R D 1976 *Rev. Mod. Phys.* **48** 239
[14] Hirshman S P and Sigmar D J 1981 *Nucl. Fusion* **21** 1079
[15] Wenzel K W and Sigmar D J 1990 *Nucl. Fusion* **30** 1117
[16] Liewer P C 1985 *Nucl. Fusion* **25** 543
[17] Wagner F and Stroth U 1993 *Plasma Phys. Control. Fusion* **35** 1321
[18] Connor J W and Wilson H R 1994 *Plasma Phys. Control. Fusion* **36** 719
[19] 2001 *Proc. 13th High Temperature Plasma Diagnostics Conf. Rev. Scientific Instrum.* **72**
[20] Forest C, Hwang Y, Ono M and Darrow D 1992 *Phys. Rev. Lett.* **68** 3559
[21] Ono M *et al* 1996 *16th IEAE Conf. IEAE-CN-64/C2-2* (Montreal, Canada: IEAE)
[22] Choe W, Ono M, Hwang Y and Chang C 1998 *Phys. Plasmas* **5** 966
[23] Menard J E 1998 *PhD Thesis* Princeton University
[24] Kaita R *et al* 2001 *Rev. Sci. Instrum.* **72** 915
[25] Isler R C 1994 *Plasma Phys. Control. Fusion* **36** 171
[26] Mattioli M *et al* 1998 *Nucl. Fusion* **38** 189
[27] Greenwald M *et al* 1988 *Nucl. Fusion* **28** 2199
[28] Murakami M, Callen J D and Berry L A 1976 *Nucl. Fusion* **16** 347
[29] Munsat T and Leblanc B 1999 *Rev. Sci. Instrum.* **70** 755
[30] Forest C B, Greene G and Ono M 1990 *Rev. Sci. Instrum.* **61** 2888
[31] Soukhanovskii V A *et al* 2001 *Rev. Sci. Instrum.* **72** 737
[32] Stutman D *et al* 1997 *Rev. Sci. Instrum.* **68** 1059
[33] Content D, Perry M E, Wroblewski D and Moos H W 1986 *Rev. Sci. Instrum.* **57** 2041
[34] Soukhanovskii V A *et al* 2001 *Rev. Sci. Instrum.* **72** 3270
[35] Hulse R A 1983 *Nucl. Technol./Fusion* **3** 259
[36] Hulse R A 1993 *Atomic and Plasma-Material Interaction Processes in Controlled Thermonucl. Fusion* ed R K Janev and H W Darwin (B. V.: Elsevier Science Publishers) p 165
[37] Galeev A A and Sagdeev R Z 1968 *Sov. Phys.* JETP **26** 233
[38] Fussman G *et al* 1991 *Plasma Phys. Control. Fusion* **33** 1677
[39] Wade M R, Houlberg W A and Baylor L R 2000 *Phys. Rev. Lett.* **84** 282
[40] Shaing K C, Hsu C T, Yokoyama M and Wakatani M 1995 *Phys. Plasmas* **2** 349
[41] Shaing K C, Yokoyama M, Wakatani M and Hsu C T 1996 *Phys. Plasmas* **3** 965
[42] Houlberg W A, Shaing K C, Hirshman S P and Zarnstorff M C 1997 *Phys. Plasmas* **4** 3230
[43] Tokar M Z *et al* 1997 *Nucl. Fusion* **37** 1691
[44] Morozov D K and Rantsev-Kartinov V A 1994 *Plasma Phys. Reports* **20** 1051
[45] Tokar M Z *et al* 1995 *Plasma Phys. Control. Fusion* **37** A241
[46] Stutman D *et al* 1999 *Plasma Phys. Control. Fusion* **41** 867
[47] Synakowski E J, Bengtson R D, Ouroua A and Wootton A J 1989 *Nucl. Fusion* **29** 311
[48] Petrasso R D *et al* 1986 *Phys. Rev. Lett.* **57** 707
[49] Haddad E, Belanger C, Gregory B C and Abel G 1992 *Plasma Phys. Control. Fusion* **34** 579
[50] Regan S *et al* 1997 *Nucl. Fusion* **37** 657
[51] Dere K P *et al* 1997 *Astron. Astrophys. Suppl. Ser.* **125** 149

[52] Landi E *et al* 1999 *Astron. Astrophys. Suppl. Ser.* **135** 339
[53] Dunseath K M *et al* 1997 *J. Phys. B: At. Mol. Opt. Phys.* **30** 277
[54] Wiese W L, Fuhr J R and Deters T M 1996 *J. Phys. Chem. Ref. Dat.* **7**
[55] International Atomic Energy Agency Nuclear Data Section, Atomic and Molecular Data Unit, Vena, Austria,http://www-amdis.iaea.org
[56] Zhang H L, Sampson D H and Fontes C J 1990 *Atomic Data and Nuclear Data Tables* **44** 31
[57] *Report* CLM-R216, Culham unpublished
[58] Burgess A 1965 *Astrophys. J.* **141** 1588
[59] Mertz A L, Cowan R D and Magee N H *Report* LA-6220-MS Los Alamos National Laboratory unpublished
[60] Arnaud M and Rothenflug R 1985 *Astron. Astrophys. Suppl. Ser.* **60** 425
[61] Mazzotta P, Mazzitelli G, Colafrancesco S and Vittorio N 1998 *Astron. Astrophys. Suppl. Ser.* **133** 403
[62] May M 2000 Johns Hopkins University private communication
[63] Menard J E *et al* 1997 *Nucl. Fusion* **37** 595
[64] Wesson J A 1995 *Plasma Phys. Control. Fusion* **37** A337
[65] Petrasso R *et al* 1981 *Nucl. Fusion* **21** 881
[66] Bombarda F *et al* 1998 *Nucl. Fusion* **38** 1861
[67] Park W and Monticello D A *Report* PPPL-2601 Princeton Plasma Physics Laboratory unpublished
[68] McGuire K and Robinson D C 1979 *Nucl. Fusion* **19** 505
[69] TFR group 1985 *Nucl. Fusion* **25** 981
[70] Seguin F H and Petrasso R 1983 *Phys. Rev. Lett.* **51** 455
[71] Ida K, Fonk R J, Hulse R A and LeBlanc B 1986 *Plasma Phys. Control. Fusion* **28** 879
[72] Hayashi T, Mazuguchi N and Sato T 1999 *26th EPS Conf. on Control. Fusion and Plasma Physics (Maastricht, 14–18 June 1999)* vol 23J (ECA) p 1361
[73] Mazuguchi N, Hayashi T and Sato T 2000 *Phys. Plasmas* **7** 940
[74] Hayashi T *et al* 2000 *Nucl. Fusion* **40** 721